

On the role of additive manufacturing, heat treatment and machining on the microstructural evolution and corrosion behaviour of AlSi9Cu3(Fe) alloy

*Original*

On the role of additive manufacturing, heat treatment and machining on the microstructural evolution and corrosion behaviour of AlSi9Cu3(Fe) alloy / Lagalante, I., Ghinatti, E., Martucci, A., Bertolini, R., Bruschi, S., Lombardi, M.. - In: MATERIALS CHARACTERIZATION. - ISSN 1044-5803. - 224:(2025). [10.1016/j.matchar.2025.115089]

*Availability:*

This version is available at: 11583/2999774 since: 2025-05-02T13:39:36Z

*Publisher:*

Elsevier

*Published*

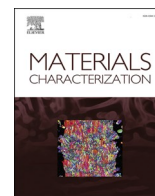
DOI:10.1016/j.matchar.2025.115089

*Terms of use:*

This article is made available under terms and conditions as specified in the corresponding bibliographic description in the repository

*Publisher copyright*

(Article begins on next page)



# On the role of additive manufacturing, heat treatment and machining on the microstructural evolution and corrosion behaviour of AlSi9Cu3 (Fe) alloy

Lagalante Ilaria<sup>a</sup>, Ghinatti Edoardo<sup>b</sup>, Martucci Alessandra<sup>a,\*</sup>, Bertolini Rachele<sup>b</sup>, Bruschi Stefania<sup>b</sup>, Lombardi Mariangela<sup>a</sup>

<sup>a</sup> Department of Applied Science and Technology, Politecnico di Torino, Corso Duca degli Abruzzi 24, 10129 Turin, Italy

<sup>b</sup> Department of Industrial Engineering, University of Padova, Via Venezia 1, 35131 Padova, Italy

## ABSTRACT

Laser Based Powder Bed Fusion for Metal (PBF-LB/M) is an additive manufacturing (AM) technique capable of producing geometrically complex, high-performance components. Among the aluminium alloys suitable for PBF-LB/M yet underexplored, AlSi9Cu3(Fe) stands out for its high strength-to-weight ratio and corrosion resistance. While the overall characteristics of AlSi9Cu3(Fe) are firmly established for cast products, studies on its mechanical performance and corrosion behaviour after the PBF-LB/M process and subsequent heat treatments remain scarce, with finishing operations often overlooked. In this framework, the paper gives novel insights into the performance of AlSi9Cu3(Fe) fabricated through a process chain comprising PBF-LB/M, heat treatment, and final machining, showing the correlation of the alloy microstructural features and surface finish with the corrosion resistance. Besides the as-built (AB) condition, two different heat treatment conditions were proposed: direct ageing (T5), and solubilisation and ageing (T6). Microstructural analysis showed that, after T5, Si network remained intact, with minor Si precipitation. On the other hand, T6 fully homogenised the microstructure, dissolving the network and activating a massive precipitation of Si, Cu and Fe phases. Afterwards, turning tests were carried out at fixed cutting parameters, showing better surface results by increasing the treatment temperatures. Potentiodynamic polarisation tests on both machined and unmachined samples gave the corrosion potential and current density at varying initial microstructural conditions. The AB samples proved to have the highest corrosion resistance before and after machining, while the lowest was always offered by the T6 samples. An explanation of such behaviour was given based on a detailed microstructural analysis together with the evaluation of the surface quality.

## 1. Introduction

Aluminium and its alloys, known for their versatility, are at the forefront of innovation in various industrial fields, from defence to automotive. Their competitive characteristics, such as low density, good mechanical properties, excellent corrosion resistance, and high thermal conductivity, have paved the way for their extensive application. In addition, their remarkable strength-to-weight ratio and impressive corrosive resistance make them an ideal alternative to heavier and more expensive metals like titanium alloys. Based on the presence and quantity of alloying elements, Al-based alloys can acquire a wide range of distinctive properties [1–3]. Silicon is a crucial alloying element in cast aluminium alloys, as it enhances fluidity and reduces solidification shrinkage, thereby improving castability [4,5]. However, cast Al–Si alloys hardly meet the industrial requirements due to their moderate strength, limited hardness, and low toughness in their as-processed state. In addition, these alloys are not well-suited for heat treatments

because the silicon in solid solution is rejected from the Al matrix at high temperatures, forming particles that rapidly grow in size and quantity, drastically reducing the alloy mechanical properties [6,7]. Nevertheless, combining small quantities of Mg in the Al–Si alloys was proved to increase mechanical performance after heat treatment thanks to the precipitation of dispersed Mg<sub>2</sub>Si nanoparticles, also improving corrosion resistance [4]. To further enhance strength and hardness, also ensuring the best mechanical performance for both heat-treated and not-treated conditions, the addition of Cu in Al–Si–Mg alloys could be the key [8–10]. Moreover, the addition of Cu provides excellent performance at higher service temperatures [1]. Another commonly added alloying element to improve the temperature performance of Al-based alloys is Fe. Nonetheless, Fe must be kept at a low percentage as it might cause a decrease in ductility and promote brittle phases that could negatively affect the material performance [3,11].

Thanks to all these possible improvements, Al–Si–Cu alloys with small quantities of Fe and Mg have been widely employed for automotive

\* Corresponding author.

E-mail addresses: [ilaria.lagalante@polito.it](mailto:ilaria.lagalante@polito.it) (L. Ilaria), [edoardo.ghinatti@phd.unipd.it](mailto:edoardo.ghinatti@phd.unipd.it) (G. Edoardo), [alessandra.martucci@polito.it](mailto:alessandra.martucci@polito.it) (M. Alessandra), [rachele.bertolini@unipd.it](mailto:rachele.bertolini@unipd.it) (B. Rachele), [stefania.bruschi@unipd.it](mailto:stefania.bruschi@unipd.it) (B. Stefania), [mariangela.lombardi@polito.it](mailto:mariangela.lombardi@polito.it) (L. Mariangela).

<https://doi.org/10.1016/j.matchar.2025.115089>

Received 26 November 2024; Received in revised form 18 March 2025; Accepted 24 April 2025

Available online 28 April 2025

1044-5803/© 2025 The Authors. Published by Elsevier Inc. This is an open access article under the CC BY license (<http://creativecommons.org/licenses/by/4.0/>).

applications, where high mechanical performance combined with light weight for reducing fuel consumption are required [12,13]. The AlSi9Cu3(Fe) (ENAC-46000) alloy is a shining example of cast Al-Si-Cu alloy successfully used in the automotive industry [14]. It offers impressive mechanical properties and good resistance to both wear and corrosion but still shows high castability and machinability [15]. According to BS EN 1706:2020 + A1:2021 standard, it boasts a tensile strength of 240 MPa, yield strength of 140 MPa, minimum elongation at fracture of 1 %, and hardness of 80 HBW. Thanks to its Cu content, the alloy retains its properties when used at higher temperatures, till 200 °C, making it suitable for engine parts. Other automotive components traditionally produced using AlSi9Cu3(Fe) include cylinder heads, pistons, shock absorbers, steering gearboxes, and heat exchangers [16,17].

Corrosion resistance is a critical factor for automotive applications, as often the components have to withstand harsh conditions, which can pose an issue in guaranteeing vehicle safety over time. In Al-Si-Cu-Fe alloys, Al noble precipitates, like  $Al_7Cu_2Fe$ ,  $Al_3Fe$ , and  $Al_2Cu$ , act as cathodic sites, leading to the formation of micro galvanic cells and preferential corrosion in the surrounding Al matrix [18]. Additionally, Si precipitates also contribute to the cathodic activity, albeit to a lesser extent than Cu- and Fe-rich phases [19]. These phases not only serve as active sites for corrosion but also prevent the formation of a protective oxide layer [20]. The negative impact of these cathodic phases increases with the heat treatment temperatures and times, as larger precipitates induce a more active matrix and result in a less protective, porous oxide layer [18,21]. Also, in [18] it was stated that the grain size influences corrosion resistance. Smaller grains are revealed to promote faster passivation. Nonetheless, once the oxide layer is breached, the high number of grain boundaries act as active sites for corrosion, promoting the propagation of deeper pits.

The vast majority of research on the corrosion resistance of AlSi9Cu3(Fe) has focused on material processed by casting or high-pressure die casting (HPDC), using a 3.5 wt% NaCl solution as corrosion medium at room temperature, according to ASTM G85 standard. The relationship between HPDC process parameters and corrosion resistance was investigated in [22], finding that a reduced porosity level improved the corrosion resistance, resulting in lower current density and higher potential. Si and Cu- and Fe- precipitates were found to stimulate micro-galvanic effects in [19] and the pitting phenomenon was time-dependent. The impact of different amounts of Cu in cast AlSi9CuX(Fe) was investigated in [14], observing slightly degrading corrosion properties as the Cu content increased from 2.2 to 4 wt%. The effect of the heat treatment on the cast AlSi9Cu3(Fe) corrosion behaviour was studied in [17], observing that the untreated samples exhibited more generalised corrosion, whereas the heat-treated ones displayed intergranular corrosion or pitting, depending on the adopted treatment time and temperature.

As seen, the mechanical properties and corrosion resistance of AlSi9Cu3(Fe) manufactured by traditional processes have received extensive attention. Nonetheless, the design limitations that characterise the traditional processes have paved the way for investigating the feasibility of using alternative and more innovative processes to fabricate AlSi9Cu3(Fe) parts. Among the promising technologies developed to overcome these limitations, the Laser Based Powder Bed Fusion for Metal (PBF-LB/M) stands out. This layer-by-layer additive manufacturing (AM) process enables the production of geometrically complex, near-net-shape metal parts with minimal porosity and enhanced properties. Nonetheless, the technology remains limited to low-volume production, because of high costs, issues related to repeatability and results consistency, and lack of proper standardisation. These issues largely impact the reliability and safety of mass production, thus limiting industrial applications and making conventional methods more cost-efficient and more suitable for large-scale manufacturing [23,24]. However, when combined with the proper design for additive manufacturing, PBF-LB/M has been shown to improve part lightweight impressively and to structurally optimise the part, thus improving the

strength-to-weight ratio. Also, its design freedom makes it ideal for customised, high-quality parts for high-end vehicles and on-demand spare parts [23,25–27].

Some studies have already attempted to process AlSi9Cu3(Fe) using PBF-LB/M. The first attempts were reported in [28], followed by studies in [12,15]. A detailed analysis of the material microstructure was conducted, reporting that the PBFed alloy shows a fine subcellular structure, with supersaturated Al matrix surrounded by a continuous network of fine Si precipitates, similar to the one seen for other Al–Si alloys [29]. Furthermore, the mechanical performance of the as-built material was compared to conventionally produced ones, i.e. HPDC [28] and as-cast [12,15], showing that, in both cases, the PBFed alloy outperformed the traditional one in both static tests, i.e. tensile and compression, and fatigue tests, thanks to a refined microstructure and lower defect density.

Heat treatments can further tailor the final mechanical performance of the PBFed alloy [30–33]. For instance, T6 treatment is a common heat treatment for aluminium alloys, consisting of three steps: a first homogenisation and phases dissolution at high temperature (solutioning), a rapid microstructural cooling that leaves the matrix supersaturated (quench) and a controlled phases precipitation (artificial ageing). It ensures an improvement in strength and hardness for Al cast alloys thanks to precipitation hardening, thus being particularly beneficial for alloys that promote precipitation hardening, like Al–Cu or Al–Mg alloys [34]. Although studies have shown that the effect of T6 treatment on PBFed Al alloys differs from that on cast alloys due to the peculiar supersaturated microstructure, it still offers important benefits. In fact, despite the potential coarsening of the fine additive microstructure at high temperatures, T6 treatment has been reported to significantly reduce material anisotropy, an important challenge in layer-by-layer technologies, while also alleviating residual stress and enhancing ductility [31,35]. Other heat treatments that better accommodate the peculiar PBFed microstructure have been investigated, such as direct ageing (T5), which is an artificial ageing at low temperatures that avoids solutioning. The treatment takes advantage of the supersaturation of the Al matrix induced by the rapid cooling of the PBF-LB/M process to promote controlled precipitation, without losing the fine microstructure or the silicon network [31]. The resulting microstructure greatly improves hardness, though usually at the expense of toughness [36–38].

The peculiar microstructural changes resulting from the high cooling rates achieved in the PBF-LB/M process can impact not only the AlSi9Cu3(Fe) mechanical and thermal properties but also its corrosion behaviour. In fact, as reported in [18,39,40], the finer grains and smaller precipitates obtained by additive process, together with the Si network that tends to limit the corrosion attack, reveal superior corrosion resistance in the PBFed alloy compared to casting. However, to the best of the authors' knowledge, the effect of heat treatments on the corrosion behaviour of PBFed AlSi9Cu3(Fe) remains unexplored, with existing studies focusing only on similar alloys. For instance, it has been observed by [41] for a PBFed AlSi10Mg treated at 300 °C, that low-temperature treatments, which lead to partial network breakage, might show deeper pitting phenomena since the broken network works as a preferential route for corrosion. On the other hand, as explored by [39] the homogenisation ensured by the T6 treatment on Al–Cu alloy leads to a uniform pitting due to the high amount of cathodic phases dispersed in the matrix that tends to guide the corrosion towards the surrounding matrix.

Another aspect that is not extensively addressed in the literature but holds significant interest for industrial applications is the effect of surface roughness resulting from AM technologies on alloy behaviour. This becomes particularly crucial for additively processed aluminium alloys, as they have been shown to exhibit the highest average surface roughness among alloys processed via PBF-LB/M [42]. Machining influences the part surface integrity, which, in turn, affects its service life performance. For instance, machining the wrought AA2024 alloy at different cutting speeds and feeds altered surface integrity characteristics such as

the severe plastic deformation layer thickness and residual stress intensity, improving fatigue resistance [43]. Similarly, surface treatments on AlSi10Mg alloy, like sandblasting, vibro-finishing, machining, and polishing, reduced roughness from 8.3 to 0.5  $\mu\text{m}$ , nearly doubling the fatigue limit from 95 to 194 MPa. In addition, several studies indicate how surface alterations induced by finishing processes can also tune the part corrosion resistance [44,45]. In [46], the surface of the wrought AA7075 alloy was plastically deformed by an ultrasonic surface rolling process, proving an increase in the part corrosion fatigue life of 26 times compared to the untreated material. Nevertheless, most of the literature studies deal with wrought and cast aluminium alloy, with only a few addressing AM alloys. In [47], AlSi10Mg samples underwent post-PBF-LB/M treatments like shot peening and ultrasonic nanocrystalline surface modification: the latter caused a change in the alloy surface integrity in terms of surface roughness, surface defects, and severe plastic deformation layer thickness that led to the decrease of wear of 80 %, decrease of corrosion current of 84 % and increase of corrosion potential of 0.1 V.

Even though profoundly innovative and promising for future developments, the corrosion resistance of the additively produced AlSi9Cu3(Fe) alloy has been rarely studied, and never in the context of a process chain that includes additive manufacturing, heat treatment, and machining. To address this literature gap, the present work aims to characterise a PBFed AlSi9Cu3(Fe) in both as-built and heat-treated conditions, and to analyse its corrosion resistance when subjected to a couple of different heat treatments and a final machining step. The study started with the microstructural analysis of the AlSi9Cu3(Fe) samples in the as-built state and different heat-treated conditions. Microstructure modifications and precipitates after each heat treatment were assessed making use of different techniques, such as differential scanning calorimetry (DSC), X-Ray diffraction (XRD), and electron backscatter diffraction (EBSD). Thereafter, the surface quality of the samples after each heat treatment was analysed before and after turning tests carried out at fixed cutting parameters. The as-built and heat-treated samples before and after machining were subjected to corrosion tests in a 3.5 wt % NaCl environment at room temperature. The correlation between microstructural features, surface quality, and corrosion resistance was finally assessed.

## 2. Materials and methods

### 2.1. Sample preparation

PBFed fully dense samples were fabricated using a commercial gas atomised AlSi9Cu3(Fe) powder provided by ECKA Granules Germany GmbH<sup>TM</sup>, with the composition reported in Table 1. The powder has a density of 2.76 g/cm<sup>3</sup>, as measured by pycnometer analysis, and a reported size range of 20–63  $\mu\text{m}$ . Further measurements conducted using a Morphologi 4 Malvern<sup>TM</sup> Panalytical assessed D10, D50, and D90 percentiles of 17.16, 32.28, and 50.24  $\mu\text{m}$  respectively, and highlighted a good, though not excellent, spherical shape of the particles. The non-perfect sphericity of the particles was then confirmed by scanning electron microscope (SEM) images (Fig. 1.a), which revealed that some particles exhibited defects, such as a high number of satellites and irregular shapes (see yellow arrows in the image).

The powder was then processed by an EOSINT M270<sup>TM</sup> Dual-mode system (EOS GmbH) in an argon atmosphere, keeping the oxygen level below 0.1 %, and using a rigid recoater. To overcome densification issues that could result from the powder defects highlighted above, a

preliminary optimisation of the process parameters was performed. The following parameters, which assured the highest level of densification, were chosen: 195 W laser power, 800 mm/s scan speed, 0.14 mm hatch distance, and 30  $\mu\text{m}$  layer thickness. The stripes scan strategy with a 67° rotation after every layer was used, and the Al-based building platform was heated at 100 °C to reduce the thermal stresses between the platform and the samples as much as possible. 10x10x10 mm<sup>3</sup> cubes were built for the material characterisation, whereas nine cylinders 25 mm high and with a diameter of 20 mm were built for the machining and corrosion tests. The cylinders were manufactured with the axis parallel to the building direction. Samples were positioned with sufficient space between each other to avoid undesirable interactions and were primarily constructed in the central area of the platform to minimise laser distortion, thereby reducing unpredictable defects. Samples were then randomly selected for the post-processes to minimise any bias in the investigation caused by building stochastic phenomena.

After the PBF-LB/M process, the as-built specimens were removed from the platform using electro-discharge machining. The Archimedes principle was applied to measure the densification level of the samples, revealing a relative density of 99.77  $\pm$  0.11 %. To evaluate the nature and size of the few porosities that were still present, an image analysis by optical microscopy OM (Leica DMI 5000 M<sup>TM</sup>) was performed, revealing a very limited number of defects (highlighted with yellow arrows in Fig. 1.b). Most of the porosities detected in the samples were identified as gas or powder-related porosities, which are very small porosities characterised by a spherical and regular shape typical of the PBF-LB/M process that usually have a limited effect on the part mechanical performance.

The samples were then subjected to two different heat treatments: (i) a solubilisation treatment, followed by water quenching and ageing (T6) and (ii) a direct ageing (T5), all performed in air. The treatment times and temperatures were selected based on the analyses conducted in [33] according to the UNI EN 1706: 2010 standard and were picked to meet possible industrial applications. Indeed, it is advisable to use heat treated alloys instead of as-built ones to ensure mechanical stability [33]. The T6 treatment described in [33] consists of a solubilisation at 520 °C for 6 h, followed by water quenching and an ageing treatment at 160 °C for 10 h. This T6 treatment is a standardised process for Al alloys, aligning with potential industrial specifications. According to [33], it enhances microstructural stability by promoting homogenisation. The resulting microstructure improves mechanical performance, offering greater toughness and enhanced stress resistance. It can also be expected that the corrosion resistance will be greatly affected by the new microstructure, as shown for similar T6 heat treated, PBFed Al alloys [39,41] having a different corrosion mechanism caused by the disappearance of the Si network.

On the other hand, T5 are treatments developed to improve the strength of PBFed alloys without overlooking the microstructure, but instead trying to accommodate it [30,31]. Indeed, [33] has reported an improvement in stress resistance, though at the expense of ductility. In particular, the hardness after treatments at three different temperatures, i.e. 140, 160, and 180 °C, at increasing holding times, were explored in [33]. The focus was on the material strengthening, identifying the treatment time needed to reach the peak hardness for each temperature, which were 26 h at 140 °C, 8.5 h at 160 °C, and 1 h at 180 °C. Then, [33] further explored the treatment at 140 °C for 26 h, which showed the highest hardness. However, in the present study, the goal is to achieve an alloy with strong mechanical properties in a practical ageing time; therefore, the T5 treatment at 160 °C for 8 h was chosen, as it also uses the same temperature as the final step of the T6 treatment. Based on [33], the microstructural changes will be limited to precipitation and possible network breakage. These small microstructural changes might however lead to important different corrosion behaviour as proved in [41] that recognise a profound pitting.

**Table 1**

Chemical composition of AlSi9Cu3(Fe) as reported by the producer ECKA Granules Germany GmbH<sup>TM</sup>.

	Si	Cu	Fe	Zn	Mg	Mn	Al
Wt%	9.3	3.0	0.91	0.81	0.29	0.21	Rem.

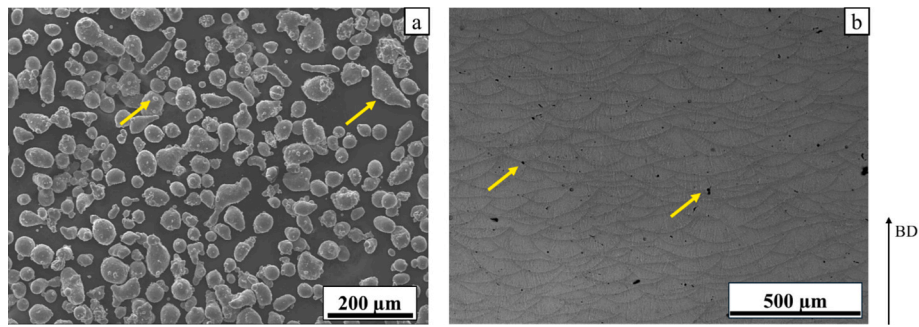


Fig. 1. (a) SEM image of the powder, highlighting irregular particles and satellites; (b) OM image of the as-built sample, taken along the building direction (z axis).

## 2.2. Material characterisation

Different characterisation techniques were used to track the changes in the material microstructure resulting from the PBF-LB/M and heat treatment steps. Image analyses of the microstructure were endured using OM and SEM (SEM EVO™ 15 for the Secondary SEM images, Phenom ProX SEM™ for the EDS analysis). The samples were etched using a Keller reagent for the SEM image analyses. The grain size distribution was measured using EBSD maps, recorded at 500× using a Tescan S9000G™ FIB-SEM. The voltage was set at 20 kV and 10 nA, with a working distance of about 7 mm and with the samples tilted 70°. The as-built and heat-treated surfaces were analysed along the building direction.

The phase identification was done using X-ray diffraction (XRD) and direct scanning calorimetry (DSC) thermal analyses. XRD was performed with a PANalytical™ X'Pert PRO PW3040/60 diffractometer, using Cu-Kα1 radiation in the angular range of 2θ from 10 to 150°, with a step size of 0.013° and a step duration of 60 s. The phase identification was done using the X'Pert HighScore software, and the fcc-Al lattice parameter was determined using the cosθcotθ method. DSC scans were conducted using a 214 Polyma™ in the temperature range between 25 and 550 °C with a heating rate of 10 °C/min. The measurements were performed in alumina crucibles under a nitrogen-protective atmosphere.

Finally, microhardness tests were performed on the XZ plane, i.e., along the building direction, using a VMHT™ Vickers tester, a static load of 0.5 kgf, and a dwell time of 10 s, following the ASTM E384 standard. Five indentations were performed for each sample for the sake of repeatability.

## 2.3. Machining trials

Longitudinal semi-finishing turning trials were conducted on an NL 1500 Mori Seiki™ CNC lathe, under conventional flooding lubrication conditions. Sandvik Coromant™ VCEX 11 03 01 L-F 1125 cutting tools were selected, whose main characteristics are reported in Table 2. Each tool was inspected before machining using a FEI™ Quanta 400 Scanning Electron Microscope to verify its integrity. The cutting parameters were kept fixed for all the experiments, being the depth of cut ( $d$ ) = 0.25 mm, cutting speed ( $V_c$ ) = 200 m/min, and feed ( $f$ ) = 0.03 mm/rev. A cutting length of 8 mm was adopted, which did not induce any noteworthy tool wear. The tool type and cutting parameters were chosen based on the recommendations of the tool manufacturer for finishing aluminium alloy parts. Three cylindrical samples were machined for each initial

Table 2  
Turning tool specifications.

Substrate	Tungsten carbide
Coating	PVD TiAlN+TiAlN
Nose radius	0.1 mm
Rake angle	5°30'
Clearance angle	7°

material state to guarantee the results repeatability.

Hereafter, the three initial material states will be referred to as AB (as-built, no heat treated), T5 (directly aged at 160 °C x 8 h), and T6 (solubilisation treated at 520 °C x 6 h, water quenched and finally aged at 160 °C x 10 h). The nomenclature of the samples prepared in this study is reported in Table 3.

## 2.4. Surface analysis

The surface topographies of the as-built and heat-treated samples were acquired before and after machining to assess the surface quality and possibly correlate the surface texture parameters and subsequent corrosion characteristics. A Sensofar Plu Neox™ 3D optical profiler (0.45 numerical aperture, maximum tilt 21°, field of view 636 × 477 μm<sup>2</sup>, spatial sampling 0.83 μm, optical resolution 0.31 μm, vertical resolution <20 nm) with a 20× Nikon™ confocal objective was used to acquire the surface topographies. Three separate areas of at least 800 × 6000 μm<sup>2</sup> were acquired for each sample. Three height surface parameters—arithmetic mean height ( $S_a$ ), kurtosis ( $S_{ku}$ ), and skewness ( $S_{sk}$ )—along with three functional parameters—core height ( $S_k$ ), reduced peak height ( $S_{pk}$ ), and reduced pit depth ( $S_{vk}$ )—were evaluated using a 2.5 μm S-filter and an 800 μm L-filter. This analysis followed ISO 25178 [48], which requires using ISO 16610 [49] for roughness computation with both the L-filter and S-filter. Both  $S_{sk}$  and  $S_{vk}$  were selected for their correlation with the amount of liquid that can be retained in the valleys of the surface topography, which in turn influences corrosion behaviour over time [44,50]. The remaining parameters were considered informative for general surface characterisation.

To evidence possible defects caused by the cutting process, the machined surfaces were qualitatively analysed by acquiring high-magnification SEM images using a backscattered electron detector (BSED). Further, the chemical composition of the machined surfaces was investigated with an Oxford Instrument™ Xplore 15 probe for energy-dispersive X-ray spectroscopy (EDS).

## 2.5. Corrosion tests

The corrosion resistance and electrochemical behaviour of the as-built and heat-treated samples before and after machining were

Table 3  
Experimental plan nomenclature.

<i>Initial material state</i>	
AB	As-built (no heat treatment)
T5	Direct ageing (160 °C/8 h)
T6	Solubilisation (520 °C/6 h) + water quenching + ageing (160 °C/10 h)
<i>Surface condition</i>	
-NM	Not machined
-PM	Post machining

evaluated via potentiodynamic polarisation (PDP) tests. After 1 h of open circuit potential (OCP) stabilization, the PDP tests were conducted using a potential range between  $-250$  mV and  $+50$  mV vs. OCP, at a scanning speed of  $0.1$  mV/s. The tests were carried out using an AMEL™ 2551 potentiostat in combination with an Ag/AgCl saturated reference electrode (ESHE =  $0.198$  V) inserted in a Luggin capillary, two platinum electrodes as the counter electrode, and an AMEL™ model 595 corrosion cell according to the ASTM G5 standard. An aqueous solution containing  $0.6$  M NaCl ( $35$  g/l L) was employed as the electrolyte, with an exposed area of  $3.67$  cm<sup>2</sup>. Each test was repeated 3 times. Before corrosion testing, the samples were ultrasonically cleaned in an acetone bath for 5 min and then dried.

The corrosion current density ( $I_{\text{corr}}$ ) and corrosion potential ( $E_{\text{corr}}$ ) were graphically extrapolated from the potentiodynamic polarisation test outcomes by using the Tafel method. The corrosion potential is a parameter commonly used to assess a metal nobleness: the higher the corrosion potential, the higher the corrosion resistance. The corrosion current density is a measure of the number of electrochemical reactions during the corrosion process, therefore the higher the corrosion current density, the higher the corrosion of the metal [51].

### 3. Results

#### 3.1. Microstructure of as-built and heat-treated alloy

The analysis of the SEM images allowed the identification of the effects of the heat treatments on the AlSi9Cu3(Fe) microstructural features and homogeneity. When examining the material along the building direction, the microstructure of the AB samples displayed the characteristic Si cellular network, already observed in other PBFed Al–Si alloys [52,53]. Additionally, fish scale-shaped melt pools were visible (Fig. 2.a). Thinner cells were observed inside the melt pools, while larger cells were recognisable at their borders (Fig. 2.b).

After the T5 heat treatment, the melt pools were still clearly visible, similar to what was seen in the AB samples (Fig. 2.d). However, at higher magnifications, it was possible to highlight how the high temperature had initiated the rupture of the Si network, which appeared irregular and broken in many different spots (Fig. 2.f). In addition, small precipitates of Si inside the Al matrix could be glimpsed, which are a result of the Si phases precipitating out of the supersaturated matrix. No Cu-phases were identified through SEM, leading to the assumption that much of Cu is still in solid solution with the aluminium and that only limited and small precipitates could have formed.

On the other hand, after the T6 heat treatment, a major difference in the microstructure was noticed. The high solubilisation temperature thoroughly homogenised the microstructure, deleting any trace of the melt pools and the cellular structure (Fig. 2.g). The subsequent ageing treatment boosted the precipitation of new phases and the growth of the already precipitated ones, as evidenced by BSED and EDS observations (Fig. 3). Si phases are sized a few micrometres and have a peculiar diamond shape, whereas minor Al-Cu/Fe phases are submicrometer and uniformly dispersed in the matrix. It can also be evidenced that a high amount of Cu is still in solid solution and has yet to precipitate. Finally, it can be observed that the T6 treatment led to more pores than the as-built and the T5 microstructures (Fig. 2.g).

Afterwards, for a better understanding of the effects of the heat treatments on the AlSi9Cu3(Fe) microstructure, EBSD analysis was conducted on the same surfaces (Fig. 4). The grain boundaries were identified by measuring the misorientation between all pixel pairs. No major differences were highlighted between the AB and T5 samples (Fig. 4.a/b). They both showed elongated grains inside the melt pools, but smaller and equiaxed ones at the borders. The presence of equiaxed grains at the melt pool bottom can be attributed to the low temperature gradient  $G$  and solidification rate  $R$  ratio ( $G/R$ ), which results from the more efficient heat conduction near the substrate and the higher solidification rate. Conversely, near the upper melt pool boundary (i.e., the interface between the solid and liquid), the formation of columnar grains is promoted by the relatively high  $G/R$  ratio [54].

The mean equivalent circular diameter (ECD) of the AB and T5 samples was  $5.42 \pm 4.43$   $\mu\text{m}$  and  $6.54 \pm 5.14$   $\mu\text{m}$ , while the maximum ECD was  $35.57$  and  $34.00$   $\mu\text{m}$ , respectively. However, by measuring the individual grains of both samples, it was found that the equiaxed grains at the melt pool borders predominantly exhibited a Feret diameter in the range of  $0.5$ – $5.0$   $\mu\text{m}$ . In contrast, the elongated grains were observed to have a Feret diameter ranging from  $50$   $\mu\text{m}$  to as much as  $100$   $\mu\text{m}$ . No preferential orientation of the grains was univocally defined. On the other hand, the T6 sample did not exhibit the bimodal grain distribution seen in the AB and T5 samples (Fig. 4.c). The grains appeared predominantly elongated, and the melt pool borders were no longer distinguishable. Only a small portion of uniformly distributed grains appeared fine (as indicated by the yellow arrow in Fig. 4.c). This phenomenon is primarily driven by the microstructural rearrangement induced by solution treatment and subsequent artificial ageing. The high solutioning temperature promotes the preferential growth of columnar grains along crystallographic directions with lower grain boundary energy. By analysing the Feret diameters obtained from the EBSD maps of

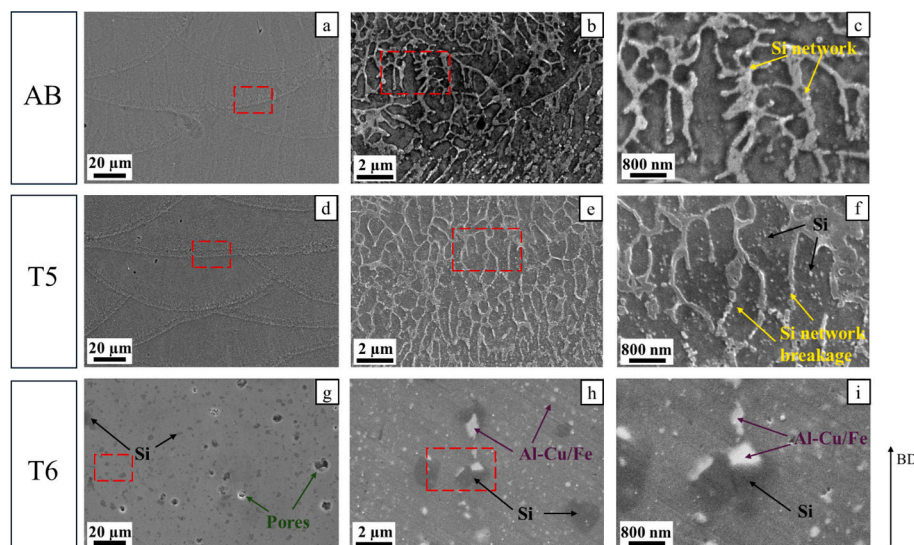


Fig. 2. Representative Secondary SEM micrographs of the AB (a-c), T5 (e-f), T6 (g-i) samples at three different magnifications ( $1500\times$ ,  $20,000\times$ ,  $50,000\times$ ).

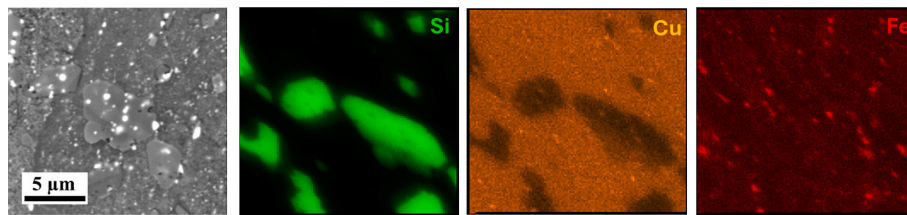


Fig. 3. BSED micrograph and EDS maps of the T6 sample.

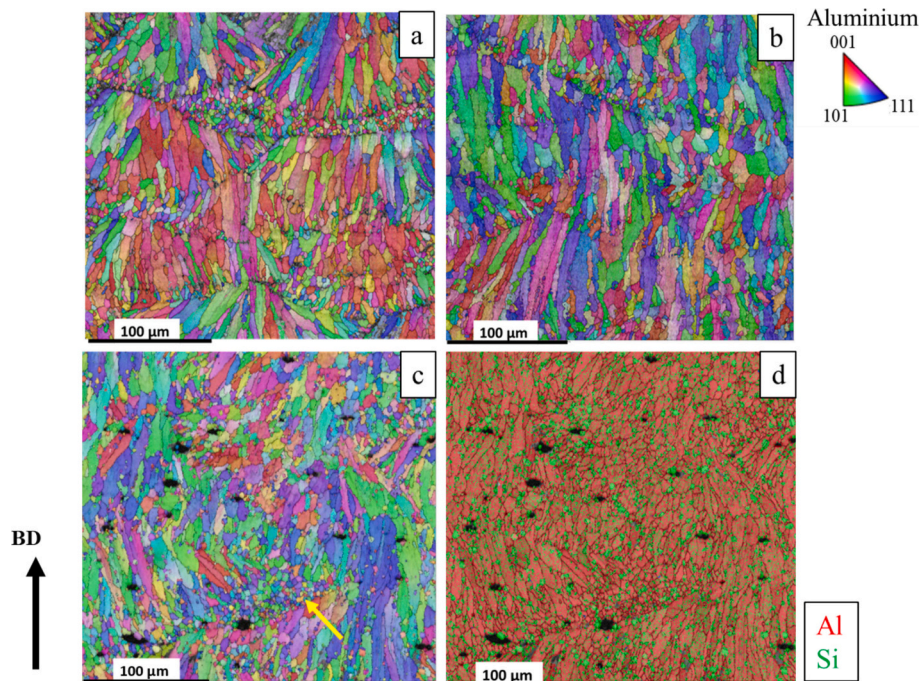


Fig. 4. EBSD images of the AB (a), T5 (b) and T6 (c) samples, at magnification 500 $\times$ ; phases analysis (d) of micrograph (c), where aluminium is in red and silicon in green. (For interpretation of the references to colour in this figure legend, the reader is referred to the web version of this article.)

T6-treated samples, it is possible to observe that grain growth has resulted in the formation of columnar grains with diameters reaching up to 250  $\mu\text{m}$ . Additionally, the phase composition was input into the Aztec<sup>TM</sup> software to map the Si precipitates, highlighting their distribution and providing the area fraction (Fig. 4.d). This analysis revealed the presence of Si where most equiaxed grains appeared, uncovering their true nature.

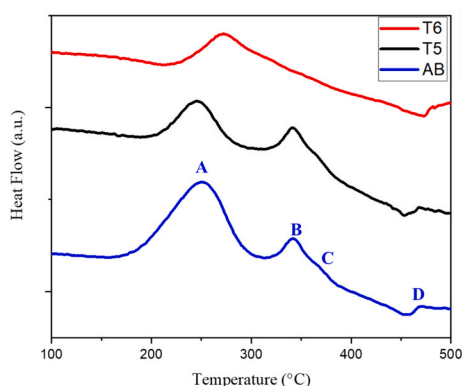


Fig. 5. DSC analysis of the AB, T5 and T6 samples.

### 3.2. Thermal analysis and phases identification

Figure 5 provides the AlSi9Cu3(Fe) thermal response in the three initial states, vertically translated to have a better comparison of the results. The AB samples showed three exothermic peaks, which can be attributed to the  $\text{Al}_2\text{Cu}$  precipitation sequence, i.e.  $\theta'' \rightarrow \theta' \rightarrow \theta$ , respectively to peaks A, B, and D. The first peak, i.e. A, is also a consequence of the diamond Si precipitation, whereas peak C can be correlated to the breaking and spheroidization of the Si network. This result is in good agreement with what was reported in [12], though in this work the last peak was noticeably less intense and started at a higher temperature. After the T5 treatment, the peak pattern remained almost unaltered, with only a slightly less intense first peak, due to ongoing stages of Si precipitation during the ageing treatment. On the other hand, after the T6 treatment, only one peak was detected, likely caused by the precipitation of the Cu remained in the solid solution. However, some studies also suggested the presence of other intermetallic phases for similar aluminium alloys, for instance by attributing the second peak of the DSC curve (B) to  $\text{Mg}_2\text{Si}$  precipitation in Al–Si alloys [55,56], but no presence of these precipitates was evidenced in this work. Nonetheless,  $\text{Mg}_2\text{Si}$  XRD patterns usually correspond to much more intense Si peaks, and precipitates might be too small and complex to spot via SEM analysis, therefore  $\text{Mg}_2\text{Si}$  presence cannot be excluded for sure. Also, the last peak of the DSC curve, which was associated with the last step of the  $\theta$ - $\text{Al}_2\text{Cu}$  precipitation sequence, might otherwise be correlated to another phase precipitation,  $\text{Al}_3\text{Fe}$ , as reported in [57] for an Al–Fe–Si alloy.

Phase identification for each initial material state was also carried out through XRD. The XRD patterns recorded for the samples in as-built and heat-treated conditions, normalised by the most intense peak, are reported in Fig. 6. The patterns of the AB and T5 samples looked very similar, showing the same peak position, though with slightly different intensities, i.e. higher Si peaks characterised the T5 samples. In both cases, high-intensity peaks of fcc-Al and diamond cubic Si were found, together with few smaller peaks associated with Al–Cu phases. The peaks were mostly in accordance with what was reported in [12]. On the other hand, higher temperature treatments led to major precipitation, revealing new secondary peaks. Indeed, after the T6 treatment, the pattern showed a much stronger signal of Si precipitates, and it also appeared richer in secondary phases, though with extremely low-intensity peaks. The tendency of Si and Cu-/Fe- phases to precipitate out of the supersaturated solution can also be seen through the measurements of the Al-lattice parameter in each condition. The measured lattice parameters for the AB, T5, and T6 samples were 4.044599, 4.045451, and 4.046245 Å, respectively. A clear increase in the parameter after each treatment can be observed.

### 3.3. Hardness

The hardness measurements give a clear understanding of how the microstructural modification after heat treatment also affects the material mechanical resistance. The hardness measurements are reported in Fig. 7. It can be noted that the T5 treatment induced a 10.4 % hardness increase compared to the AB state. On the other hand, after the T6 treatment, the material showed almost the same hardness as in the as-built condition but a 7.3 % decrease relative to T5. It was also observed that the standard deviation in the T6 sample is significantly lower compared to those measured in the AB and T5 samples.

### 3.4. Surface finish before machining

Figure 8.a illustrates the height surface roughness parameters of AlSi9Cu3(Fe) samples before machining. The surface is generally very rough, with Sa values exceeding 10 µm for all samples analysed. The Sa values indicate that the T5 sample exhibits the highest roughness, while both AB and T6 show a slight reduction. The Sku values remain relatively consistent across all conditions, slightly decreasing from AB to T6 but remaining above 3, indicating a surface with sharp features. Similarly, the Ssk values stay near zero in all conditions, suggesting a symmetric distribution of peaks and valleys.

Figure 8.b presents the functional surface roughness parameters for the AlSi9Cu3(Fe) samples before machining. Sk is the highest for the T5 condition, indicating a significant material plateau that dominates the surface profile. Both the AB and T6 conditions exhibit slightly lower and

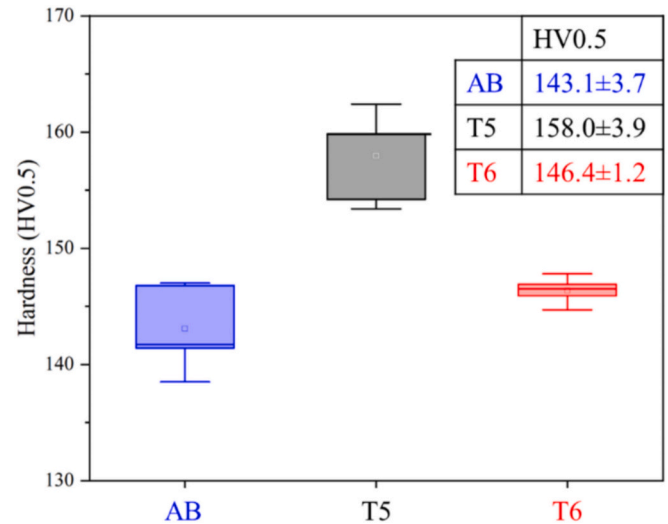


Fig. 7. Hardness of the AB, T5 and T6 samples.

comparable Sk values, suggesting a smoother surface with a less pronounced core roughness.

The Spk values indicate that the AB has the highest peak height, while heat treatment reduces this value, with T5 showing a moderate decrease and T6 exhibiting the lowest Spk. This suggests that heat treatment, particularly T6, helps in reducing the prominence of surface peaks. The Svk values, which represent valley depths, remain relatively stable across all conditions, with only a slight reduction in T5 and T6. The limited change in Svk indicates that heat treatment primarily affects surface peaks rather than deep valleys.

### 3.5. Corrosion behaviour before machining

Figure 9.a and b present the OCP and PDP curves before machining, respectively, corresponding to different initial microstructural states. From Fig. 9.a, it is evident that the corrosion potential is influenced by the initial microstructural state of the AlSi9Cu3(Fe) alloy. For the AB and T5 samples, the OCP values fluctuated within a 30 mV range before reaching equilibrium. In contrast, the T6 samples exhibited a higher initial OCP value, followed by a 100 mV drop before stabilising. This suggests greater electrochemical instability in the T6 samples compared to the AB and T5 samples, whose OCP curves showed smaller fluctuations.

Figure 9.b confirms that the cathodic and anodic branches of the AB and T5 samples demonstrated a higher degree of linearity, whereas the T6 samples exhibited fluctuations in both the cathodic and anodic

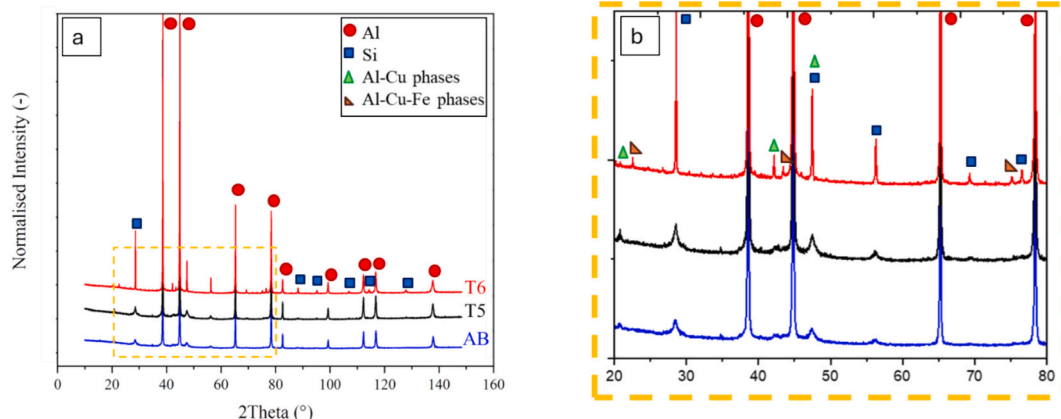


Fig. 6. XRD patterns of the AB, T5 and T6 samples (a); zoom of the patterns between 20 and 80°, for better readability.

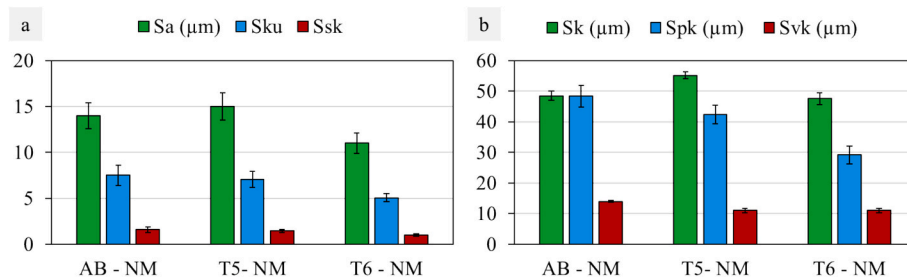


Fig. 8. a) Height surface roughness parameters and b) functional surface roughness parameters of the AB, T5, and T6 samples before machining.

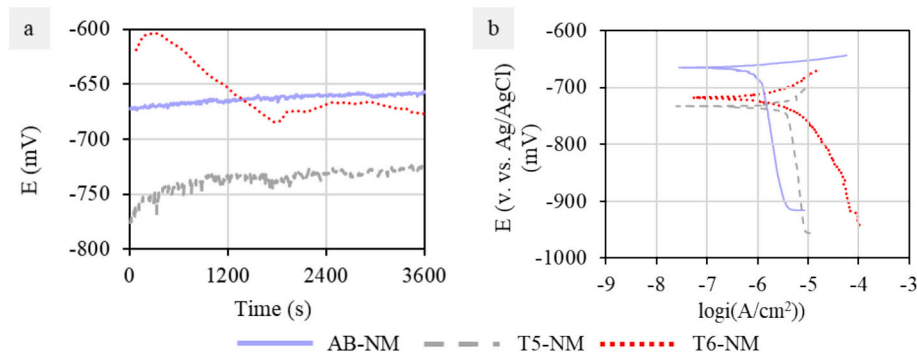


Fig. 9. OCP (a) and PDP curves (b) of the AB, T5, and T6 samples before machining.

regions, suggesting a less stable electrochemical behaviour.

Figure 10 presents the corrosion potential and the corrosion current density as functions of the material initial state, derived from the PDP curves. The AB samples exhibited the highest corrosion potential, indicating superior corrosion resistance. In contrast, the T5 and T6 samples showed lower corrosion potential values, with a reduction in  $E_{corr}$  of 10.3 % and 7.5 %, respectively. A similar trend is observed for  $I_{corr}$ , as shown in Fig. 10.b, although the differences are significantly more pronounced:  $I_{corr}$  increases by 146.2 % and 151.8 % for the T5 and T6 samples, respectively, compared to the AB ones.

### 3.6. Surface finish after machining

The height surface roughness parameters after machining are presented in Fig. 11.a. The  $S_a$  values reveal that the AB condition exhibits the highest surface roughness, indicating a more irregular texture compared to the T5 and T6 samples, which have slightly lower  $S_a$  values. Among them, the T6 condition demonstrates the smoothest surface, while T5 displays a slightly higher roughness.

The  $S_{sk}$  parameter provides additional insight into the surface profile. Both AB and T5 exhibit negative skewness, indicating that their surfaces are dominated by deep valleys rather than pronounced peaks, with T5 showing the most pronounced effect. In contrast, the T6

condition presents a slightly positive skewness, which is characteristic of turned surfaces, suggesting that it features more elevated peaks than valleys.

The  $S_{ku}$  values remain consistently above 3 across all conditions, confirming a leptokurtic distribution, which is indicative of sharp peaks and deep valleys rather than a uniformly distributed surface profile.

Figure 11.b presents the functional surface roughness parameters for the AlSi9Cu3(Fe) samples in the AB, T5, and T6 conditions after machining. The  $S_k$  values indicate that the AB condition has the highest  $S_k$ , closely followed by T5, while the T6 samples exhibit significantly lower  $S_k$  values, indicating a smoother and more uniform core surface.

The  $S_{pk}$  values, which represent the prominence of surface peaks, follow a consistent trend across all conditions, with AB and T6 exhibiting comparable values, while T5 shows the lowest peak prominence, implying that the T5 surface has fewer protruding asperities.

In contrast,  $S_{vk}$  values follow a different trend. The AB condition exhibits the highest  $S_{vk}$ , indicating deep valleys that may increase susceptibility to localised corrosion. The T5 condition shows slightly lower  $S_{vk}$  values, while the T6 condition has the shallowest valleys.

The error bars indicate considerable variability in  $S_k$  for the AB and T5 conditions, suggesting inconsistencies in the material plateau structure. However,  $S_{vk}$  and  $S_{pk}$  values show more stable trends across all conditions.

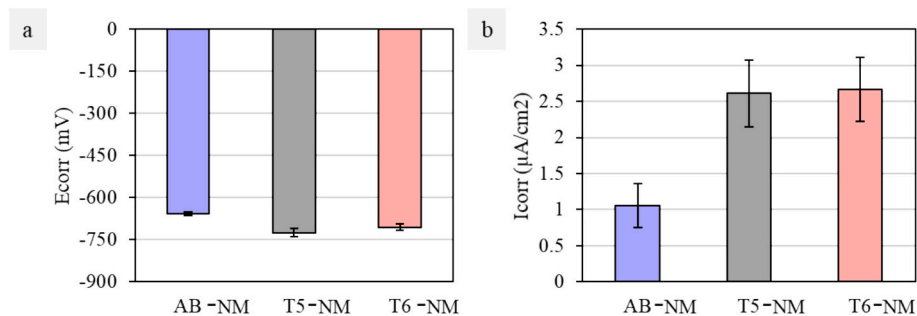


Fig. 10.  $E_{corr}$  (a) and  $I_{corr}$  (b) of the AB, T5, and T6 samples before machining.

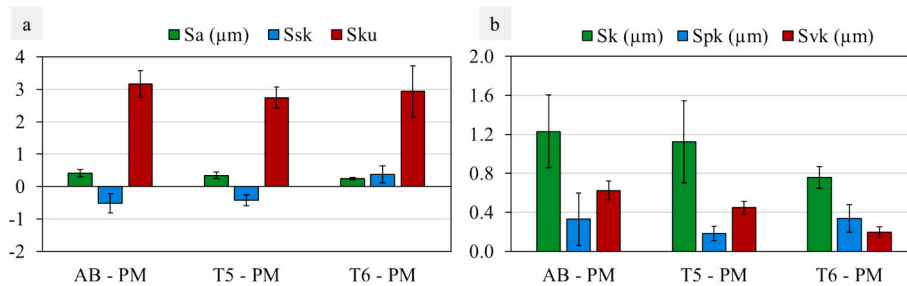


Fig. 11. a) Height surface roughness parameters and b) functional surface roughness parameters of the AB, T5, and T6 samples after machining.

Comparing the results of Fig. 11 with those of Fig. 8, it is evident that the machining process led to a significant reduction in all roughness parameters considered, contributing to an overall smoother surface across all conditions.

Fig. 12 presents high-magnification SEM images combined with EDS maps showing the Si distribution on the sample surfaces after machining. Feed marks, characteristic of the turning process, were visible regardless of the material initial microstructural state. Various surface defects were detectable, but their morphology and density depended on the sample’s initial microstructural state: the machined surfaces of the AB and T5 samples were characterised by a uniform distribution of tears, even if the AB surfaces had a higher concentration of tears compared to the T5 ones. On the contrary, the T6 surfaces did

not exhibit tears, but a distribution of micro-holes, which can be ascribed to both the detachment of Si precipitates from the aluminium matrix due to turning and the pores generated by the T6 heat treatment (Fig. 12.e). The EDS maps showed an even distribution of Si (in green) on the surfaces of the AB and T5 samples, while, on the T6 surface, the presence of Si precipitates was visible.

### 3.7. Corrosion behaviour after machining

Figure 13.a presents the OCP after machining for different initial microstructural states. The overall OCP trend over time remains consistent with the one before machining, with the T6 samples exhibiting high variability and instability. After stabilization, the T5 and T6

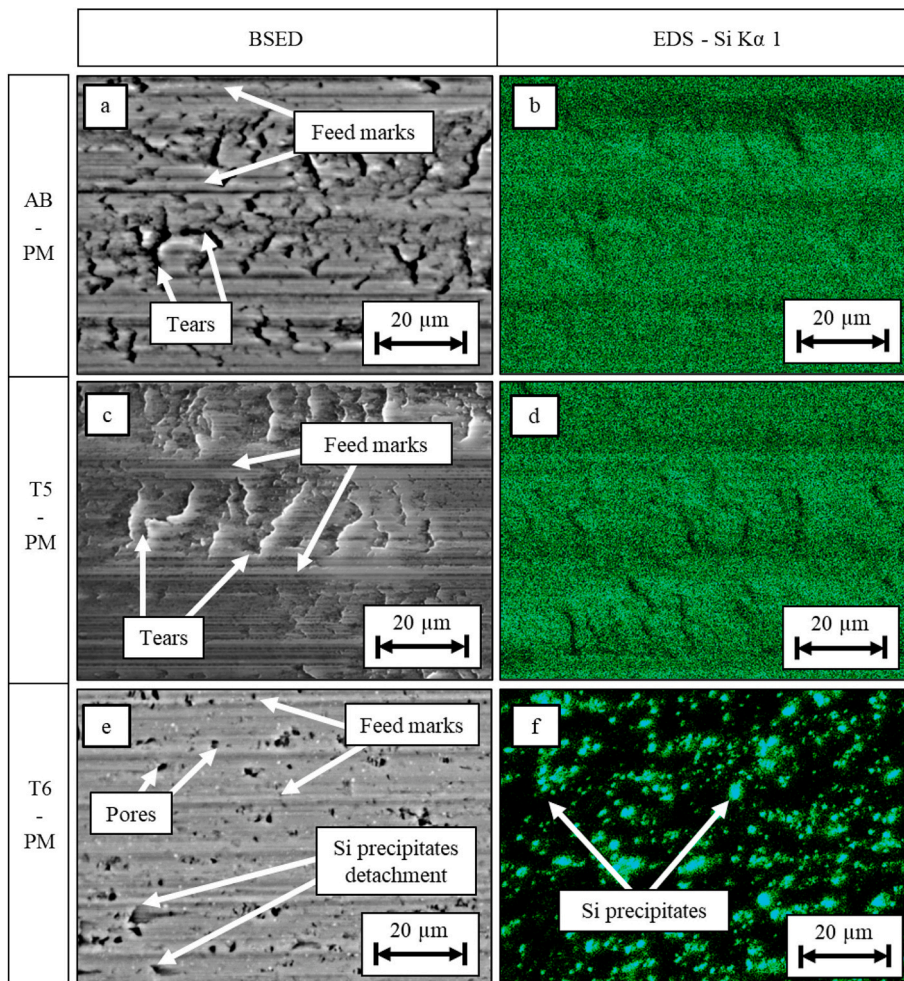


Fig. 12. SEM images of the machined surfaces of the AB, T5, and T6 samples at 2500× magnification (a), (c), and (e); EDS maps to evidence the Si distribution (b), (d), and (f).

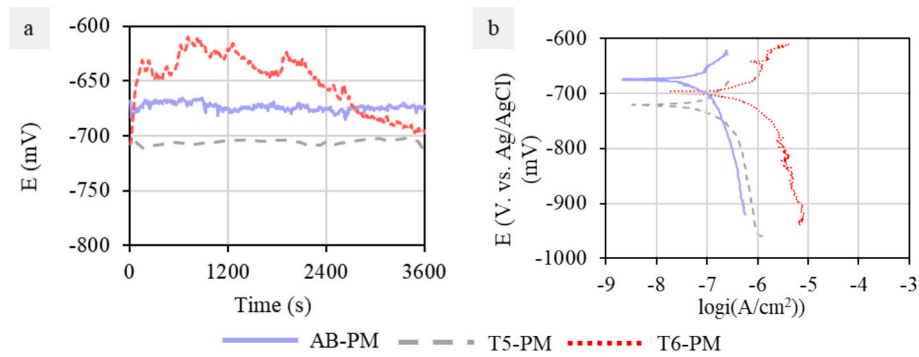


Fig. 13. OCP (a) and PDP curves (b) of the AB, T5, and T6 samples after machining.

samples reach similar OCP values, while the AB samples consistently maintain the most noble potential.

Figure 13.b presents the PDP curves for different initial microstructural states after machining, while the corresponding values extracted from these curves are summarised in Fig. 14.

Comparing these values with those reported in Section 3.5, it can be inferred that the surface modifications induced by machining had a minimal effect on the corrosion potential. In other words, even a significant improvement in surface finish due to machining did not influence the corrosion potential whatever the material microstructural state is.

Conversely, machining had a pronounced impact on the corrosion current density. Specifically, machining reduced the corrosion current density by one order of magnitude for the AB and T5 samples, while for the T6 samples, the reduction was smaller, reaching 24 %.

## 4. Discussion

### 4.1. Effect of the heat treatment on the microstructure and corrosion behaviour

The high cooling rates characterising the AM processes, particularly the PBF-LB/M one, induce a distinctive microstructure in the Al-Si-Cu-Fe alloys [58]. The rapid solidification leads to the formation of a supersaturated solid solution, as the elevated cooling rates significantly enhance the solid solubility of solute elements, preventing the typical formation of equilibrium phases. Consequently, the microstructure is exceptionally fine, characterised by features that are not typically observed in conventionally processed alloys [9,55,59]. Indeed, a very fine cellular structure was observed within the melt pools, indicative of this rapid solidification dynamics (Fig. 2.c). These fine cells were especially prominent in the central region of the melt pools. However, the microstructure changed at the borders, where multiple melt pools overlap, and larger cells are formed, reflecting variations in thermal gradients and cooling rates during the process [52]. Interestingly, very few secondary phases could be spotted since the high cooling rates also

suppress the formation of secondary phases. This was particularly noticeable since Cu and Fe are present, largely remaining in supersaturated solid solution instead of precipitating as distinct secondary phases, as also demonstrated by the absence of secondary peaks in the XRD pattern (Fig. 6). This suppression of secondary phase formation contributes to the unique mechanical and physical properties of the PBF-LB/M processed AlSi9Cu3(Fe) alloy, offering a material that combines fine microstructural features with a high degree of solute retention.

Preliminary microstructural investigations conducted at low magnification on the samples subjected to the T5 treatment revealed that the low temperature involved in this treatment did not induce significant changes in the overall microstructure. The original melt pool shapes and the interconnected Si network remained distinctly visible, indicating that the as-built microstructure was largely preserved (Fig. 2.d). Also, as visible in Fig. 4, no significant changes in the grain distribution and size could be observed after the heat treatment. Nonetheless, closer examinations at higher magnifications highlighted how the T5 ageing temperature was enough to initiate localised precipitation of Si inside the aluminium matrix and to induce partial breakage of the Si network (Fig. 2.f). These changes were particularly pronounced in the heat-affected zones and at melt pool borders, where the thermal gradients during processing are more variable and emphasized. The DSC and XRD analyses further evidenced the higher presence of Si precipitates resulting from this precipitation process. Indeed, the DSC analysis (Fig. 5) revealed a notably smaller peak associated with the Si precipitation in the T5 samples compared to the as-built one, indicating that a significant portion of the Si had already precipitated during the T5 treatment, thus reducing the amount available for further precipitation during the DSC measurement. Additionally, the XRD analysis (Fig. 6) showed that the peaks corresponding to Si appear more intense in the T5 sample compared to the as-built one. This increased peak intensity reflects a higher degree of Si precipitation. Furthermore, the measured Al lattice parameter increased after the T5 treatment, implying the precipitation of Si and possibly other elements like Cu and Fe out of the supersaturated solution during the heat treatment. This behaviour is consistent with the fact that elements like Si, Cu, and Fe reduce the

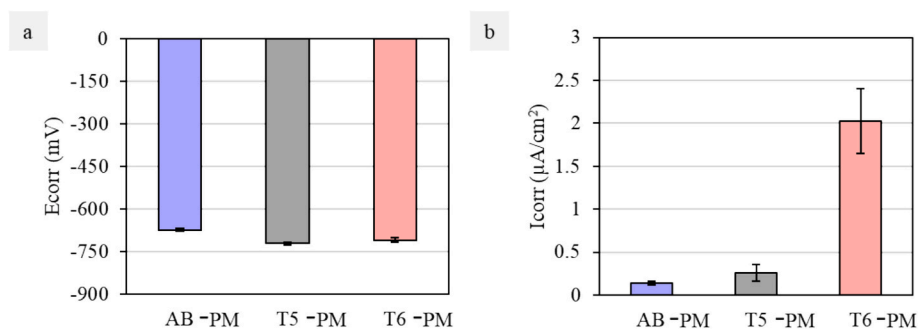


Fig. 14. Corrosion potential (a) and corrosion current density (b) of the AB, T5, and T6 samples after machining.

lattice spacing when dissolved in aluminium but cause an increase in the lattice parameter upon precipitation due to their smaller atomic radii relative to aluminium [60,61]. However, no significant differences in the formation of other secondary phases were observed between the AB and T5 samples. The XRD patterns showed no new peaks, and the SEM image analysis did not reveal any additional phases. This might suggest that the low ageing temperature of the T5 treatment was insufficient to activate the precipitation of other secondary phases. However, it is also plausible that precipitation takes place, but Cu and Fe-rich phases remain in a particularly low amount and nanometric size, not allowing them to be detected by image analysis nor by XRD, since peaks can be clearly distinguished in the XRD pattern only when in an amount of at least 5 % [62].

The T5 heat treatment is typically applied to enhance the mechanical properties of the aluminium alloys. Indeed, this low-temperature treatment facilitates controlled precipitation of solute elements, which contributes to an increase in material strength via precipitation hardening. Importantly, this process achieves a balance, allowing the material to gain strength through secondary phases without compromising the beneficial effects of the PBF-LB/M peculiar fine microstructure, contributing to its overall strengthening [53,63]. The effectiveness of the T5 treatment in enhancing hardness was demonstrated by the increased hardness values reported in Fig. 7, which shows a 10.4 % increase in hardness compared to the AB state. This increase is directly related to the finely dispersed Si precipitates (Fig. 2.f), which obstruct dislocation movement, thereby enhancing the material resistance to deformation. The hardness measurements provide a clear understanding of how microstructural modifications induced by heat treatment influence the mechanical resistance of the material and also provide insight into the material yield strength, as the literature suggests a well-established correlation between these two properties, typically governed by a factor of approximately 1/3 [64]. Given these results, it can be reasonably hypothesised that the T5 treatment will significantly improve tensile strength due to the finer and more dispersed precipitation.

The precipitation of Si precipitates and the Si network partial breakage resulting from the T5 treatment are also known to influence the material corrosion behaviour [41]. The intact Si network in the as-built condition generally acts as a barrier to corrosion because it forms and maintains the oxide layer which protects the Al matrix, effectively containing and limiting the spread of corrosive agents within the material, contributing to the overall stability of the as-built condition corrosion resistance, as indicated by the OCP curves shown in Fig. 9.a. On the contrary, when the Si network is disrupted during heat treatment, it creates pathways that facilitate corrosion progression. These broken network regions also have a less stable oxide layer, which prevents protection from corrosion and further serves as preferential routes for corrosive species to penetrate deeper into the alloy, lowering the corrosion potential and increasing the corrosion current density compared to the as-built condition (Fig. 10). Since the Al matrix has a lower concentration of Si, the Si particles can act as micro-galvanic cells within the Al matrix. In these cells, the Al matrix, being more anodic, tends to corrode preferentially compared to the Si precipitates, which are more cathodic [20].

The microstructure of the PBFed AlSi9Cu3(Fe) alloy underwent a significant transformation after the T6 heat treatment, displaying characteristics that were markedly different from those observed in the as-built and T5-treated conditions. The T6 samples did not show the distinctive melt pool shapes, and the Si network, which was prominent in the previous microstructures, was no longer visible (Fig. 2.g). This change directly results from the high solubilisation temperature, which aims to homogenise the Al matrix, followed by the controlled precipitation and growth of various phases during the subsequent ageing process. During the T6 treatment, a complete Si precipitation from the supersaturated solid solution was witnessed, as also confirmed by the absence of the Si precipitation peak during the DSC analysis (Fig. 5). The

precipitates grew to sizes ranging from several nanometres to a few micrometres, but uniformly dispersed throughout the microstructure (Fig. 2.h, 3). In addition to the larger Si precipitates, new smaller phases emerged, as detected through both image analysis (Fig. 3) and then confirmed by the XRD patterns (Fig. 6). These phases were primarily identified as intermetallic compounds, including  $\theta$ -Al<sub>2</sub>Cu and Al-Fe (—Cu) minor phases. However, the small size and relatively low volume fraction of these intermetallic compounds pose challenges for detection via XRD, as their diffraction signals are often weak and may overlap with those of more dominant phases like the Al and Si ones, potentially obscuring their detection. This overlap complicates the unambiguous identification of specific phases. However, based on previous research on PBFed AlSi9Cu3(Fe) [33], it can be hypothesised that these minor phases might be the cathodic phases Al<sub>5</sub>FeSi, Al<sub>7</sub>Cu<sub>2</sub>Fe, or Al<sub>8</sub>Fe<sub>5</sub>. The higher precipitation of both Si and minor elements rich in Cu and Fe could also be inferred from the increase of the Al lattice parameter, which implied further precipitation of Si, Cu, and Fe elements out of supersaturated solution. However, it must also be observed that a high amount of Cu can still be observed inside the matrix: its higher presence in solid solution could also be inferred from the DSC curve after T6 (Fig. 5). Indeed, the presence of the exothermic peak correlated to Al—Cu precipitation confirms that during T6, though already partially precipitated, Cu still remains in solid solution. The high temperature involved in the T6 treatment also led to a significant homogenisation of grain structure. The pronounced difference between the elongated grains within the melt pools and the fine equiaxed grains at the melt pool boundaries, which is characteristic of the as-built condition, became nearly indistinguishable after the T6 treatment (Fig. 4). However, a notable downside of the T6 treatment was the increased porosity observed within the alloy (Fig. 2.g). This phenomenon was already reported in previous research on Al alloys [33,55,65,66]. The origin of this porosity has not been uniquely and entirely understood. It is mainly associated with the incipient melting of Al—Cu phases during the high-temperature treatment [33,55,67] and the expansion of gases trapped in pre-existing pores [66,68,69]. The increase in porosity can have a detrimental effect on the part performance, potentially compromising its mechanical resistance. Additionally, the presence of pores can severely impact the material corrosion resistance, as these voids can act as initiation sites for corrosion, facilitating the inlet of corrosive agents and accelerating the degradation process.

The T6 treatment also ensured a slight improvement in hardness compared to the AB condition (Fig. 7), though showing only a 2.3 % increase, and a 7.3 % decrease relative to T5. The lone solubilisation step would lead to a decrease in strength and hardness, as reported for an Al-Si-Mg-Cu alloy in [55], due to the massive Si precipitation out of the supersaturated solution (Fig. 3) and the growth of the fine microstructure, which led to the near disappearance of equiaxed grain boundaries and a general coarsening of the grains (Fig. 2.h, 4.c), thus causing the loss of several strengthening mechanism, i.e. the contribution of supersaturation, dislocation and grain boundaries. However, during the ageing treatment, the controlled precipitation of different phases improved the precipitation strengthening contribution, recovering the as-built strength. It can also be noted that the hardness standard deviation was the lowest in the T6 samples compared to the AB and T5 states, thanks to the high homogenisation and uniform dispersion of the precipitates obtained during the solubilisation process, which weakened the microstructural anisotropy, thus resulting in more consistent mechanical properties. As previously stated, hardness behaviour is linked to the material yield strength; thus, the T6 treatment may lead to a reduction in yield strength compared to the AB. However, the coarsening of the grains achieved after T6 treatment will probably contribute to a reduction in strength and an increase in elongation [64].

The T6 treatment also significantly influenced the material corrosion behaviour due to its peculiar microstructure, which foresees the complete dissolution of the Si network. With the Si network dissolved, the alloy becomes more prone to forming a less protective oxide layer,

making it more susceptible to corrosion attacks. Notably, the partial or complete dissolution of the Si network observed in the T5 and T6 samples, respectively, has a similar impact on corrosion current density (Fig. 14b). This suggests that the integrity of the Si network plays a key role in determining the corrosion resistance of the AlSi9Cu3(Fe) alloy.

#### 4.2. Effect of machining on the corrosion behaviour

After machining, the surfaces of the AB and T5 samples were characterised by a significant density of tears (Fig. 12.a,12.c) as a consequence of their highly inhomogeneous microstructure with fine cellular structure within the melt pools and coarser one near the boundaries, which induced local variations in the resistance the tool encountered when cutting the material [70]. Nevertheless, the T5 samples exhibited fewer tears and higher surface finish quality than the AB ones as a consequence of the microstructure modification induced by the Si network fragmentation at the melt pool boundaries and the formation of Si precipitates [31]. The similar cutting response exhibited by the AB and T5 samples is attributed to forming a similar surface texture, which shows comparable roughness levels. Increased variability is observed compared to T6 samples, arising from the stochastic nature of the tearing process, which introduces random surface irregularities.

On the contrary, the machining of the T6 samples resulted in a less rough surface, due to the profoundly different microstructure resulting from the heat treatment they underwent compared to the AB and T5 samples (Fig. 11). The heat treatment homogenised the microstructure, dissolving the Si network and promoting a uniform distribution of the Si precipitates along with the Fe and Cu phases. This homogeneous microstructure offered less resistance to cutting, hence inducing a less defective surface. The Si precipitation was much more substantial in the T6 samples, with a bigger size of precipitates on average compared to the other two microstructural conditions (Fig. 2). Since the interface between the Al matrix and the precipitates is weaker than the matrix itself, the action of the cutting tool could facilitate the Si precipitates detachment (Fig. 12.e) [71].

The machining step did not affect the corrosion potential of AlSi9Cu3(Fe), regardless of the material initial microstructural state (Fig. 14.a). The corrosion potential values remained largely unchanged compared to the pre-machining condition (Fig. 10.a), despite the significantly improved surface finish of all machined samples. This behaviour can be attributed to the fact that corrosion potential is a thermodynamic parameter, primarily governed by the material chemical composition and electrolyte chemistry, rather than surface roughness. Corrosion potential is determined by the electrochemical equilibrium between anodic and cathodic reactions. While increased surface roughness may enhance reaction rates, it affects both anodic and cathodic processes proportionally, maintaining a relatively stable corrosion potential.

Conversely, the machining step significantly influenced the corrosion current density of AlSi9Cu3(Fe), regardless of the material initial microstructural state (Fig. 14.b). Corrosion current density is a kinetic parameter directly affected by the electrochemically active surface area, which increases with surface roughness.

It is acknowledged that surface roughness directly influences the contact area between the electrolyte and the part surface: the lower the roughness, the smaller the contact area [72], which, in turn, reduces the number of electrochemical reactions occurring between the electrolyte and the material. However, in the present study, no clear correlation was found between surface texture parameters and corrosion indicators. Notably, a rougher surface, such as that of the AB samples, did not correspond to poorer corrosion resistance. This observation also extends to Svk and Ssk, surface texture parameters specifically related to corrosion, as they represent the depth of surface valleys and the number of valleys, respectively, which can trap corrosive agents and promote localised corrosion. Despite having the lowest Svk, the T6 samples exhibited the worst corrosion performance, particularly in terms of corrosion current density.

However, surface roughness alone is not the only factor influencing corrosion behaviour as the type of surface defects must also be considered. The AB samples still exhibited the lowest corrosion current density, with the T5 ones having a slightly higher value. Despite the AB and T5 samples having higher roughness, they are characterised by the same type of surface defects, namely tearing, which may explain the unexpected trend observed in the T5 samples before and after machining.

In contrast, the T6 samples, despite having the smoothest surface, exhibited the highest corrosion current density. This is attributed to the morphology of their surface defects, specifically the detachment of the Si precipitates, which creates small pits on the surface (Fig. 12.e). These pits likely act as localised corrosion initiation sites, accelerating the overall corrosion rate. Furthermore, the limited reduction in Icorr between the states before and after machining can be attributed to the presence of voids within the material even before machining (Fig. 2.g). These voids behave similarly to the micro-holes formed during the machining process.

Thus, it can be stated that the corrosion behaviour of AlSi9Cu3(Fe) after machining is primarily governed by a combination of microstructural characteristics and surface defect morphology rather than surface roughness alone.

## 5. Conclusions

The study explores the effects of different heat treatments on the microstructure of an AlSi9Cu3(Fe) alloy produced through PBF-LB/M, and how the different microstructures influence the surface finish and the corrosion resistance. Three main conditions were considered for the heat treatments and turning tests: as-built (not heat treated), T5 (direct ageing), and T6 (solubilisation + water quenching + ageing).

The main results can be summarised as follows:

- The high cooling rates of the PBF-LB/M process induce a distinctive microstructure, characterised by super-saturated solid solution, fine cellular structure, fine grains and recognisable melt pool shape.
- The lower temperature T5 heat treatment maintains the melt pool shapes and the as-built cellular microstructure. However, temperature activates network breakage and small-sized Si precipitation, which enhances hardness though affecting the overall galvanic effect.
- The three-step T6 heat treatment leads to a full homogenisation of the alloy, the complete precipitation of Si phases and of other minor ones out of the supersaturated solid solution. Melt pool shapes are also no longer visible. The uniform distribution of precipitates induces precipitation strengthening, making up for the loss of solid solution strengthening. Corrosion is affected by the increase in phases that promote galvanic corrosion, also weakening the protective oxide layer. In addition, an increase in porosity was detected.
- The corrosion resistance of AlSi9Cu3(Fe) shows that the AB condition exhibits the best corrosion behaviour due to its microstructure, characterised by an integral Si network. Conversely, the dissolution of this network leads to a deterioration in corrosion performance, particularly in terms of corrosion current density.
- Turning tests on PBF-LB/M cylinders of AlSi9Cu3(Fe) alloy before and after heat treatment was performed. The T6 samples after machining resulted in the best surface roughness, even if their surface was dominated by micro-holes due to SiC detachment. The turned surfaces of the AB and T5 samples were instead dominated by tearing, with the former showing the worst surface roughness and the latter settling in between the surface roughness of the AB and T6 samples.
- The corrosion current density of AlSi9Cu3(Fe) improves after machining due to the reduction in surface roughness, while, in contrast, the corrosion potential remains unaffected by machining. Besides the microstructure induced by heat treatment, which still plays a significant role, surface defects resulting from machining

become another highly influential factor. The AB and T5 samples, with a surface initially dominated by tearing, stabilise at the same corrosion current, whereas T6, with a surface primarily characterised by micro-holes, exhibits the worst performance.

### CRedit authorship contribution statement

**Lagalante Ilaria:** Writing – original draft, Investigation, Formal analysis, Data curation. **Ghinatti Edoardo:** Writing – original draft, Investigation, Formal analysis, Data curation. **Martucci Alessandra:** Writing – review & editing, Visualization, Validation, Supervision, Methodology. **Bertolini Rachele:** Writing – review & editing, Visualization, Validation, Supervision, Methodology. **Bruschi Stefania:** Writing – review & editing, Supervision, Resources, Funding acquisition, Conceptualization. **Lombardi Mariangela:** Writing – review & editing, Supervision, Resources, Funding acquisition, Conceptualization.

### Declaration of competing interest

The authors declare that they have no known competing financial interests or personal relationships that could have appeared to influence the work reported in this paper.

### Acknowledgements

This work was financed by the European Union – Next Generation EU (National Sustainable Mobility Center CN00000023, Italian Ministry of University and Research Decree n. 1033 - 17/06/2022, Spoke 11 - Innovative Materials & Lightweighting). The opinions expressed are those of the authors only and should not be considered representative of the European Union or the European Commission's official position. Neither the European Union nor the European Commission can be held responsible for them.

### Data availability

Data will be made available on request.

### References

- [1] R.S. Rana, Rajesh Purohit, S. Das, Reviews on the influences of alloying elements on the microstructure and mechanical properties of aluminum alloys and aluminum alloy composites, *Int. J. Sci. Res. Publ.* 2 (6) (2012) 1–7.
- [2] O.S.I. Fayomi, A.P.I. Popoola, N.E. Udoye, Effect of alloying element on the integrity and functionality of aluminium-based alloy, in: S. Sivasankaran, A. C. di (Eds.), *Aluminium Alloys - Recent Trends in Processing, Characterization, Mechanical Behavior and Applications*, InTech, 2017, <https://doi.org/10.5772/intechopen.71399>.
- [3] B. Callegari, T.N. Lima, R.S. Coelho, The influence of alloying elements on the microstructure and properties of Al-Si-based casting alloys: a review, *Metals* 13 (7) (2023) 1174, <https://doi.org/10.3390/met13071174>.
- [4] G. Niu, Y. Wang, L. Zhu, J. Ye, J. Mao, Fluidity of casting Al-Si series alloys for automotive light-weighting: a systematic review, *Mater. Sci. Technol.* 38 (13) (2022) 902–911, <https://doi.org/10.1080/02670836.2022.2068274>.
- [5] M.L. Montero-Sistiaga, et al., Changing the alloy composition of Al7075 for better processability by selective laser melting, *J. Mater. Process. Technol.* 238 (2016) 437–445, <https://doi.org/10.1016/j.jmatprotec.2016.08.003>.
- [6] K.G. Prashanth, et al., Microstructure and mechanical properties of Al-12Si produced by selective laser melting: effect of heat treatment, *Mater. Sci. Eng. A* 590 (2014) 153–160, <https://doi.org/10.1016/j.msea.2013.10.023>.
- [7] S. Hegde, K.N. Prabhhu, Modification of eutectic silicon in Al-Si alloys, *J. Mater. Sci.* 43 (9) (2008) 3009–3027, <https://doi.org/10.1007/s10853-008-2505-5>.
- [8] F. Bosio, P. Fino, D. Manfredi, M. Lombardi, Strengthening strategies for an Al alloy processed by in-situ alloying during laser powder bed fusion, *Mater. Des.* 212 (2021) 110247, <https://doi.org/10.1016/j.matdes.2021.110247>.
- [9] A. Martucci, E. Bassini, M. Lombardi, Effect of Cu content on the PBF-LB/M processing of the promising Al-Si-Cu-Mg composition, *Metals* 13 (7) (2023) 1315, <https://doi.org/10.3390/met13071315>.
- [10] G. Wang, X. Bian, W. Wang, J. Zhang, Influence of Cu and minor elements on solution treatment of Al-Si-Cu-Mg cast alloys, *Mater. Lett.* 57 (24–25) (2003) 4083–4087, [https://doi.org/10.1016/S0167-577X\(03\)00270-2](https://doi.org/10.1016/S0167-577X(03)00270-2).
- [11] J.A. Taylor, Iron-containing intermetallic phases in Al-Si based casting alloys, *Procedia Mater. Sci.* 1 (2012) 19–33, <https://doi.org/10.1016/j.mspro.2012.06.004>.
- [12] J. Fiocchi, C.A. Biffi, A. Tuissi, Selective laser melting of high-strength primary AlSi9Cu3 alloy: processability, microstructure, and mechanical properties, *Mater. Des.* 191 (2020) 108581, <https://doi.org/10.1016/j.matdes.2020.108581>.
- [13] M. Zhang, Y. Tian, X. Zheng, Y. Zhang, L. Chen, & J. Wang, «Research progress on multi-component alloying and heat treatment of high strength and toughness Al-Si-Cu-Mg cast aluminum alloys», *Materials*, vol. 16, fasc. 3, p. 1065, 2023, doi: <https://doi.org/10.3390/ma16031065>.
- [14] M. Voncina, A. Nagode, M. Bizjak, Dependence of mechanical properties on Cu content in AlSi9Cu3(Fe) alloy, *Teh. Vjesn. - Tech. Gaz.* 24 (Supplement 1) (2017), <https://doi.org/10.17559/TV-20140922143741>.
- [15] J. Suchy, L. Pantelejev, D. Paloušek, D. Koutný, J. Kaiser, Processing of AlSi9Cu3 alloy by selective laser melting, *Powder Metall.* 63 (3) (2020) 197–211, <https://doi.org/10.1080/00325899.2020.1792675>.
- [16] F. Sanna, A. Fabrizi, S. Ferraro, G. Timelli, P. Ferro, & F. Bonollo, «Multiscale Characterisation of AlSi9Cu3(Fe) die Casting Alloys after Cu, Mg, Zn and Sr Addition», fasc. 4 n.d.
- [17] N. Zazi, Effect of heat treatments on the microstructure, hardness and corrosion behavior of nondendritic AlSi9Cu3(Fe) cast alloy, *Mater. Sci.* 19 (3) (2013) 258–263, <https://doi.org/10.5755/j01.ms.19.3.1397>.
- [18] R.A. Michi, A. Plotkowski, A. Shyam, R.R. Dehoff, S.S. Babu, Towards high-temperature applications of aluminium alloys enabled by additive manufacturing, *Int. Mater. Rev.* 67 (3) (2022) 298–345, <https://doi.org/10.1080/09506608.2021.1951580>.
- [19] C. Monticelli, F. Zanotto, A. Balbo, V. Grassi, A. Fabrizi, G. Timelli, Corrosion behavior of high-pressure die-cast secondary AlSi9Cu3(Fe) alloy, *Corros. Sci.* 209 (2022) 110779, <https://doi.org/10.1016/j.corsci.2022.110779>.
- [20] D. Culliton, A.J. Betts, D. Kennedy, Impact of intermetallic precipitates on the tribological and/or corrosion performance of cast aluminium alloys: a short review, *Int. J. Cast Met. Res.* 26 (2) (2013) 65–71, <https://doi.org/10.1179/1743133612Y.0000000038>.
- [21] R. Revilla, D. Verkens, T. Rubben, & I. De Graeve, «Corrosion and corrosion protection of additively manufactured aluminium alloys—a critical review», *Materials*, vol. 13, fasc. 21, p. 4804, ott. 2020, doi: <https://doi.org/10.3390/ma13214804>.
- [22] S.L. Dos Santos, R.A. Antunes, S.F. Santos, Influence of injection temperature and pressure on the microstructure, mechanical and corrosion properties of a AlSiCu alloy processed by HPDC, *Mater. Des.* 88 (2015) 1071–1081, <https://doi.org/10.1016/j.matdes.2015.09.095>.
- [23] A. Hamza, K. Bousnina, I. Dridi, N. Ben Yahia, Revolutionizing automotive design: the impact of additive manufacturing, *Vehicles* 7 (1) (2025) 24, <https://doi.org/10.3390/vehicles7010024>.
- [24] H.Y. Ma, et al., Advances in additively manufactured titanium alloys by powder bed fusion and directed energy deposition: microstructure, defects, and mechanical behavior, *J. Mater. Sci. Technol.* 183 (2024) 32–62, <https://doi.org/10.1016/j.jmst.2023.11.003>.
- [25] «Latest Ferrari and McLaren supercars feature structural AM components», *Metal Add. Manufact.* n.d.
- [26] E. Bassoli, S. Defanti, E. Tognoli, N. Vincenzi, L. Degli Esposti, Design for additive manufacturing and for machining in the automotive field, *Appl. Sci.* 11 (16) (2021) 7559, <https://doi.org/10.3390/app11167559>.
- [27] N. Zhao, et al., Direct additive manufacturing of metal parts for automotive applications, *J. Manuf. Syst.* 68 (2023) 368–375, <https://doi.org/10.1016/j.jmsy.2023.04.008>.
- [28] M. Fousova, D. Dvorsky, M. Vronka, D. Vojtech, P. Lejcek, The use of selective laser melting to increase the performance of AlSi9Cu3Fe Alloy, *Materials* 11 (10) (2018) 1918, <https://doi.org/10.3390/ma11101918>.
- [29] R. Casati, M. Coduri, S. Checchia, M. Vedani, Insight into the effect of different thermal treatment routes on the microstructure of AlSi7Mg produced by laser powder bed fusion, *Mater. Charact.* 172 (2021) 110881, <https://doi.org/10.1016/j.matchar.2021.110881>.
- [30] H.R. Kotadia, G. Gibbons, A. Das, P.D. Howes, A review of laser powder bed fusion additive manufacturing of aluminium alloys: microstructure and properties, *Addit. Manuf.* 46 (2021) 102155, <https://doi.org/10.1016/j.addma.2021.102155>.
- [31] J. Fiocchi, A. Tuissi, C.A. Biffi, Heat treatment of aluminium alloys produced by laser powder bed fusion: a review, *Mater. Des.* 204 (2021) 109651, <https://doi.org/10.1016/j.matdes.2021.109651>.
- [32] J. Fiocchi, et al., Heat treatments for stress relieving AlSi9Cu3 alloy produced by laser powder bed fusion, *Materials* 14 (15) (2021) 4184, <https://doi.org/10.3390/ma14154184>.
- [33] M. Roudnická, O. Molnárová, D. Dvorský, L. Krivský, D. Vojtěch, Specific response of additively manufactured AlSi9Cu3Fe alloy to precipitation strengthening, *Met. Mater. Int.* 26 (8) (2020) 1168–1181, <https://doi.org/10.1007/s12540-019-00504-y>.
- [34] Heat Treating of Aluminum Alloys, *ASM Handbook*, Vol. 4: Heat Treating ASM Handbook Committee, p 841–879 n.d. DOI: <https://doi.org/10.1361/asmhba0001205>.
- [35] W. Li, et al., Effect of heat treatment on AlSi10Mg alloy fabricated by selective laser melting: microstructure evolution, mechanical properties and fracture mechanism, *Mater. Sci. Eng. A* 663 (2016) 116–125, <https://doi.org/10.1016/j.msea.2016.03.088>.
- [36] M. Fousová, D. Dvorský, A. Michalčová, D. Vojtěch, Changes in the microstructure and mechanical properties of additively manufactured AlSi10Mg alloy after exposure to elevated temperatures, *Mater. Charact.* 137 (2018) 119–126, <https://doi.org/10.1016/j.matchar.2018.01.028>.

- [37] R. Casati, M. Coduri, M. Riccio, A. Rizzi, M. Vedani, Development of a high strength Al-Zn-Si-Mg-Cu alloy for selective laser melting, *J. Alloys Compd.* 801 (2019) 243–253, <https://doi.org/10.1016/j.jallcom.2019.06.123>.
- [38] J.T. Oliveira De Menezes, E.M. Castrodeza, R. Casati, Effect of build orientation on fracture and tensile behavior of A357 Al alloy processed by selective laser melting, *Mater. Sci. Eng. A* 766 (2019) 138392, <https://doi.org/10.1016/j.msea.2019.138392>.
- [39] S. Lorenzi, et al., Corrosion behavior assessment of an Al-Cu alloy manufactured via laser powder bed fusion, *Corros. Sci.* 227 (2024) 111698, <https://doi.org/10.1016/j.corsci.2023.111698>.
- [40] M. Fousova, V. Valesova, D. Vojtech, Corrosion of 3D-printed AlSi9Cu3Fe alloy, *Manuf. Technol.* 19 (1) (2019) 29–36, <https://doi.org/10.21062/ujep/240.2019/a/1213-2489/MT/19/1/29>.
- [41] T. Rubben, R.I. Revilla, I. De Graeve, Influence of heat treatments on the corrosion mechanism of additive manufactured AlSi10Mg, *Corros. Sci.* 147 (2019) 406–415, <https://doi.org/10.1016/j.corsci.2018.11.038>.
- [42] A. Martucci, A. Aversa, & M. Lombardi, «Ongoing challenges of laser-based powder bed fusion processing of Al alloys and potential solutions from the literature—a review», *Materials*, vol. 16, 3, p. 1084, gen. 2023, doi: <https://doi.org/10.3390/ma16031084>.
- [43] H. Chen, Z. Liu, X. Wang, Y. Wang, S. Liu, Effect of surface integrity on fatigue life of 2024 aluminum alloy subjected to turning, *J. Manuf. Process.* 83 (2022) 650–666, <https://doi.org/10.1016/j.jmapro.2022.07.070>.
- [44] R. Bertolini, L. Lizzul, L. Pezzato, A. Ghiotti, S. Bruschi, Improving surface integrity and corrosion resistance of additive manufactured Ti6Al4V alloy by cryogenic machining, *Int. J. Adv. Manuf. Technol.* 104 (5–8) (2019) 2839–2850, <https://doi.org/10.1007/s00170-019-04180-5>.
- [45] M. Sadeghi, A. Diaz, P. McFadden, E. Sadeghi, Chemical and mechanical post-processing of alloy 718 built via electron beam-powder bed fusion: surface texture and corrosion behavior, *Mater. Des.* 214 (2022) 110405, <https://doi.org/10.1016/j.matdes.2022.110405>.
- [46] X. Xu, D. Liu, X. Zhang, C. Liu, D. Liu, W. Zhang, Influence of ultrasonic rolling on surface integrity and corrosion fatigue behavior of 7B50-T7751 aluminum alloy, *Int. J. Fatigue* 125 (2019) 237–248, <https://doi.org/10.1016/j.ijfatigue.2019.04.005>.
- [47] E. Maleki, O. Unal, M. Bandini, M. Guagliano, S. Bagherifard, Individual and synergistic effects of thermal and mechanical surface post-treatments on wear and corrosion behavior of laser powder bed fusion AlSi10Mg, *J. Mater. Process. Technol.* 302 (2022) 117479, <https://doi.org/10.1016/j.jmatprotec.2021.117479>.
- [48] ISO 25178-2:2022 Geometrical Product Specifications (GPS). Surface texture: Areal. Terms, Definitions and Surface Texture Parameters, ISO, Brussels, Belgium. n.d.
- [49] EN ISO 16610-61:2015 Geometrical Product Specification (GPS). Filtration. Linear Areal Filters. Gaussian Filters, ISO, Brussels, Belgium. n.d.
- [50] S. Bruschi, R. Bertolini, A. Ghiotti, E. Savio, W. Guo, R. Shivpuri, Machining-induced surface transformations of magnesium alloys to enhance corrosion resistance in human-like environment, *CIRP Ann.* 67 (1) (2018) 579–582, <https://doi.org/10.1016/j.cirp.2018.04.040>.
- [51] F. Li, et al., Controllable precipitation behavior near grain boundaries enabled by artificial strain concentration in age-hardening aluminum alloys, *Mater. Sci. Eng. A* 892 (2024) 146026, <https://doi.org/10.1016/j.msea.2023.146026>.
- [52] N.T. Aboulkhair, N.M. Everitt, I. Ashcroft, C. Tuck, Reducing porosity in AlSi10Mg parts processed by selective laser melting, *Addit. Manuf.* 1–4 (2014) 77–86, <https://doi.org/10.1016/j.addma.2014.08.001>.
- [53] R. Casati, M. Vedani, Aging response of an A357 Al alloy processed by selective laser melting, *Adv. Eng. Mater.* 21 (4) (2019) 1800406, <https://doi.org/10.1002/adem.201800406>.
- [54] J. Wang, R. Zhu, Y. Liu, L. Zhang, Understanding melt pool characteristics in laser powder bed fusion: an overview of single- and multi-track melt pools for process optimization, *Adv. Powder Mater.* 2, fasc. 4 (2023) 100137, <https://doi.org/10.1016/j.apmate.2023.100137>.
- [55] F. Bosio, I. Lagalante, D. Manfredi, M. Lombardi, Bespoke multi-step homogenization heat-treatment for a laser powder bed fused AlSi10Mg4Cu alloy synthesized via in-situ alloying, *Mater. Charact.* 195 (2023) 112506, <https://doi.org/10.1016/j.matchar.2022.112506>.
- [56] R.H. Kemsies, B. Milkereit, S. Wenner, R. Holmestad, O. Kessler, In situ DSC investigation into the kinetics and microstructure of dispersoid formation in Al-Mn-Fe-Si-(Mg) alloys, *Mater. Des.* 146 (2018) 96–107, <https://doi.org/10.1016/j.matdes.2018.03.007>.
- [57] N. J. Luiggi A, «A preliminary study of the phase transformations in rolled Al-Fe-Si alloy», *Metall. Mater. Trans. A*, vol. 41, fasc. 13, pp. 3271–3275, 2010, doi: <https://doi.org/10.1007/s11661-010-0496-8>.
- [58] X.P. Li, et al., A selective laser melting and solution heat treatment refined Al–12Si alloy with a controllable ultrafine eutectic microstructure and 25% tensile ductility, *Acta Mater.* 95 (2015) 74–82, <https://doi.org/10.1016/j.actamat.2015.05.017>.
- [59] P. Rometsch, Q. Jia, K.V. Yang, X. Wu, Aluminum alloys for selective laser melting – Towards improved performance, in: *Additive Manufacturing for the Aerospace Industry*, Elsevier, 2019, pp. 301–325, <https://doi.org/10.1016/B978-0-12-814062-8.00016-9>.
- [60] A.M. Samuel, H.W. Doty, S. Valtierra, F.H. Samuel, Defects related to incipient melting in Al–Si–Cu–Mg alloys, *Mater. Des.* 1980–2015 52 (2013) 947–956, <https://doi.org/10.1016/j.matdes.2013.05.048>.
- [61] M. Draissia, M.-Y. Debili, Study of solid-solution hardening in binary aluminium-based alloys, *Open Phys.* 3 (3) (2005) 395–408, <https://doi.org/10.2478/BF02475646>.
- [62] E.J. Mittemeijer, P. Scardi, A. c. di, *Diffraction Analysis of the Microstructure of Materials*, in: Springer Series in Materials Science vol. 68, Springer Berlin Heidelberg, Berlin, Heidelberg, 2004, <https://doi.org/10.1007/978-3-662-06723-9>.
- [63] Q. Jia, P. Rometsch, S. Cao, K. Zhang, & X. Wu, «Towards a high strength aluminium alloy development methodology for selective laser melting», *Mater. Des.*, vol. 174, p. 107775, lug. 2019, doi: <https://doi.org/10.1016/j.matdes.2019.107775>.
- [64] M.F. Ashby, H. Shercliff, D. Cebon, *Materials: Engineering, Science, Processing and Design, Third edition, North American edition, Elsevier Butterworth-Heinemann, Amsterdam; Boston; Heidelberg ; London, 2014.*
- [65] F. Bosio, C. Phutela, N. Ghisi, A. Alhammadi, N.T. Aboulkhair, Tuning the microstructure and mechanical properties of AlSi10Mg alloy via in-situ heat-treatments in laser powder bed fusion, *Mater. Sci. Eng. A* 879 (2023) 145268, <https://doi.org/10.1016/j.msea.2023.145268>.
- [66] S.J. Hirsch, L. Winter, T. Grund, T. Lampke, Heat treatment influencing porosity and tensile properties of field assisted sintered AlSi7Mg0.6, *Materials* 15 (7) (2022) 2503, <https://doi.org/10.3390/ma15072503>.
- [67] B. Andilab, C. Ravindran, N. Dogan, A. Lombardi, G. Byczynski, In-situ analysis of incipient melting of Al2Cu in a novel high strength Al-Cu casting alloy using laser scanning confocal microscopy, *Mater. Charact.* 159 (2020) 110064, <https://doi.org/10.1016/j.matchar.2019.110064>.
- [68] K. Riener, T. Pfalz, F. Funcke, G. Leichtfried, Processability of high-strength aluminum 6182 series alloy via laser powder bed fusion (LPBF), *Int. J. Adv. Manuf. Technol.* 119 (7–8) (2022) 4963–4977, <https://doi.org/10.1007/s00170-022-08673-8>.
- [69] X.P. Li, K.M. O'Donnell, T.B. Sercombe, Selective laser melting of Al-12Si alloy: enhanced densification via powder drying, *Addit. Manuf.* 10 (2016) 10–14, <https://doi.org/10.1016/j.addma.2016.01.003>.
- [70] S. Bruschi, R. Bertolini, A. Ghiotti, H. Mahmood, C. Zanella, Machinability of recycled aluminum alloys, *Manuf. Lett.* 41 (2024) 1669–1675, <https://doi.org/10.1016/j.mfglet.2024.09.194>.
- [71] Y. Bai, et al., Unique cellular microstructure-enabled hybrid additive and subtractive manufacturing of aluminium alloy mirror with high strength, *J. Mater. Process. Technol.* 320 (2023) 118095, <https://doi.org/10.1016/j.jmatprotec.2023.118095>.
- [72] P. Jan, B. Žugelj, M. Kalin, In-situ micro-asperity investigation of real contact area formation during sliding with the effects of roughness and normal load considered, *Tribol. Int.* 191 (2024) 109171, <https://doi.org/10.1016/j.triboint.2023.109171>.